

Evidence for Fe-Si-O liquid immiscibility at deep Earth pressures

Sarah M. Arveson^{a,1}, Jie Deng^a, Bijaya B. Karki^b, and Kanani K. M. Lee^a

^aDepartment of Geology & Geophysics, Yale University, New Haven, CT 06511; and ^bSchool of Electrical Engineering & Computer Science, Department of Geology & Geophysics, Center for Computation and Technology, Louisiana State University, Baton Rouge, LA 70803

Edited by Ho-kwang Mao, Carnegie Institution for Science, Washington, DC, and approved April 16, 2019 (received for review December 20, 2018)

Seismic observations suggest that the uppermost region of Earth's liquid outer core is buoyant, with slower velocities than the bulk outer core. One possible mechanism for the formation of a stably stratified layer is immiscibility in molten iron alloy systems, which has yet to be demonstrated at core pressures. We find immiscibility between liquid Fe-Si and Fe-Si-O persisting to at least 140 GPa through a combination of laser-heated diamond-anvil cell experiments and first-principles molecular dynamics simulations. High-pressure immiscibility in the Fe-Si-O system may explain a stratified layer atop the outer core, complicate differentiation and evolution of the deep Earth, and affect the structure and intensity of Earth's magnetic field. Our results support silicon and oxygen as coexisting light elements in the core and suggest that SiO₂ does not crystallize out of molten Fe-Si-O at the core-mantle boundary.

high pressure | melting | alloys | core composition

S ilicon, oxygen, sulfur, carbon, and hydrogen have long been proposed as light element candidates that make up the $\sim 10\%$ density deficit between iron and the iron–light element mixture that composes Earth's outer core (1, 2). Silicon has long been a favorable candidate due to its high solubility in iron in a wide range of pressure and temperature conditions (e.g., ref. 3) and geochemical arguments (4). Oxygen is a likely light element candidate because it is the most abundant element in the bulk silicate Earth and partitions strongly into liquid iron (5). Additionally, first-principles computations suggest that the presence of oxygen is required to produce densities and compressional wave velocities matching those of the outer core (6).

Despite the lines of evidence favoring silicon and oxygen in the core, a recent experimental study observed that SiO₂ crystallizes out of molten Fe-Si-O alloys at high pressures until either all of the silicon or oxygen is exhausted in the melt (7). This would imply that silicon and oxygen cannot coexist in the liquid outer core and hence cannot both be major light elements in the outer core. Based on those experiments, it was speculated that SiO₂ crystallizes out of nearly the entire Fe-Si-O ternary system at core—mantle boundary (CMB) thermodynamic conditions. However, no other evidence, experimental or otherwise, supports SiO₂ crystallization to be thermodynamically favorable in the Fe-Si-O system at high pressures.

We investigated molten Fe-Si-O alloys between 13 GPa and 78 GPa at temperatures up to 4,000 K in a laser-heated diamond-anvil cell (LHDAC) (*SI Appendix*, Fig. S1). We performed ex situ textural and chemical analyses to identify whether quenched melt blebs were composed of immiscible Fe-Si and Fe-Si-O or a single Fe-Si-O composition. We performed first-principles molecular dynamics (FPMD) simulations on the Fe-Si-O system at conditions relevant to our experiments to confirm immiscibility between liquid Fe-Si and Fe-Si-O. We also performed FPMD simulations at outer core pressures to extrapolate the experimental results and to reproduce the closure of the miscibility gap with temperature.

We used Fe-Si-O alloys of 0.5–3 wt% O and 8–9 wt% Si (*SI Appendix*, Table S1). These compositions fit well within predictions for core composition based on recent metal–silicate

equilibration in a deep magma ocean (8) and on modeling of accretion and differentiation (9). The composition also lies within the range predicted for SiO_2 crystallization used in a previous study (7).

We find that the molten Fe-Si-O alloys exhibit two-phase immiscibility up to at least 78 GPa. The miscibility gap is temperature dependent, and the transition from two immiscible liquids to one miscible liquid is apparent in quenched texture (Fig. 1). Nearly all of the oxygen partitions into one phase forming an Fe-Si-O melt, and the second phase is an Fe-Si melt (Fig. 2). The resulting microstructure in quenched samples takes one of two forms: a dispersed microstructure (Fig. 1C) when the melt is quenched from a temperature high enough so that the Fe-Si and Fe-Si-O melts are miscible (Fig. 3) or an egg-type core microstructure (Fig. 1D) (10) when the melt is quenched in the immiscible region (Fig. 3). The dispersed microstructure is characteristic of spinodal decomposition (11). Fig. 1 shows the evolution of quenched texture with temperature. The Fe-9wt%Si-3wt%O sample was heated in four spots. Spot 1 was heated to a peak temperature below the melting curve of Fe-Si9wt% (12). Spots 2 and 3 were heated above the melting curve to peak temperatures of 2,850 K and 2,840 K, respectively, and exhibit two immiscible liquids: an Fe-Si core and an Fe-Si-O shell (Fig. 1 B and D). Spot 4 was heated to a peak temperature of 3,100 K and shows quenched exsolution texture from miscible phases (Fig. 1C). This temperature-dependent evolution of quenched texture and composition is evident throughout the pressure range we investigate, 13-78 GPa. We found two immiscible liquids in samples whether they were heated using a salt or using a noble gas for thermal insulation. Samples melted

Significance

Earth's outer core is composed of a liquid iron alloy with up to 10% of unknown light elements, likely silicon, oxygen, sulfur, carbon, or hydrogen. The release of these light elements upon freezing of the solid iron inner core plays an important role in sustaining Earth's magnetic field, but the exact chemical makeup of the core is widely debated. In this paper, we perform high-pressure, high-temperature melting experiments and first-principles simulations on iron alloys containing silicon and oxygen and find that two distinct liquids form at high pressures. The presence of immiscible liquids may explain a seismically observed stratified layer atop the outer core and suggests that an Fe-Si-O composition can explain multiple observations of the outer core.

Author contributions: S.M.A. and K.K.M.L. designed research; S.M.A. and K.K.M.L. performed experiments; J.D. and B.B.K. performed computations; S.M.A., J.D., B.B.K., and K.K.M.L. analyzed data; and S.M.A., J.D., B.B.K., and K.K.M.L. wrote the paper.

The authors declare no conflict of interest.

This article is a PNAS Direct Submission

Published under the PNAS license.

¹To whom correspondence should be addressed. Email: sarah.arveson@yale.edu.

This article contains supporting information online at www.pnas.org/lookup/suppl/doi:10.1073/pnas.1821712116/-/DCSupplemental.

Published online May 8, 2019.

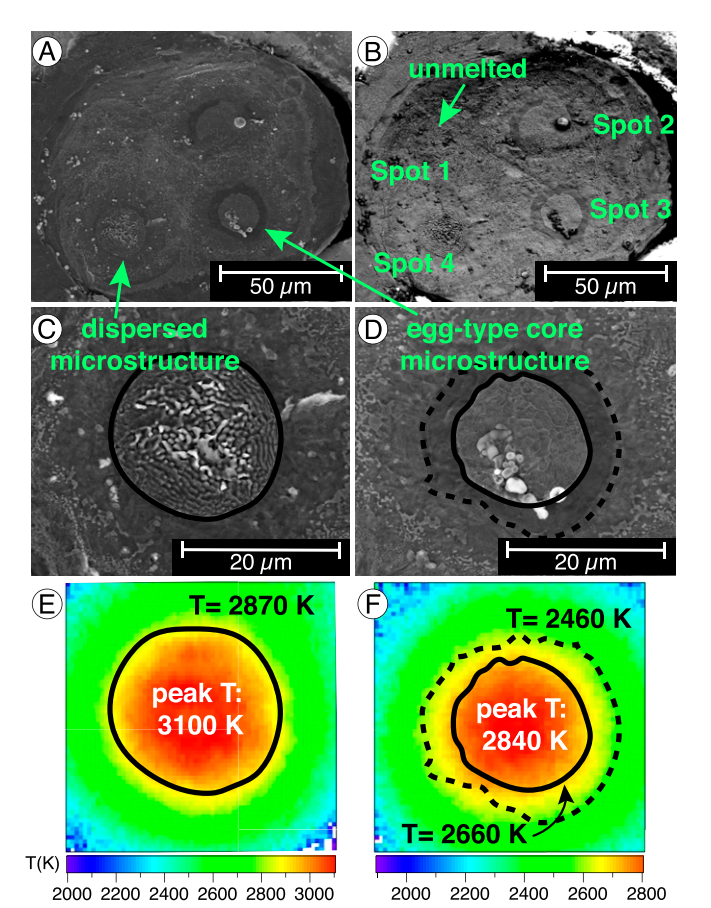


Fig. 1. (*A* and *B*) SEM image using (*A*) secondary electrons and (*B*) back-scattered electrons of an Fe-9wt%Si-3wt%O sample, FeSi913(s3, s4) heated at 31 GPa in four spots at different temperatures. (*C*) Spot 4: Dispersed microstructure is observed at high temperatures exceeding 2,870 K after being quenched from miscible melts. (*D*) Spot 3: Egg-type core microstructure is observed. The inner region contains an oxygen-depleted Fe-Si melt, and the shell contains an oxygen-enriched Fe-Si-O melt. (*E* and *F*) Temperature maps for (*E*) spot 4 and (*F*) spot 3. Contours of varied texture are shown in corresponding temperature maps.

using noble gas Ar as insulation show a much smoother and more elevated melt bleb; however, when polished in cross-section, the egg-type core microstructure is evident (*SI Appendix*, Fig. S2). The quenched Fe-Si and Fe-Si-O molten regions show homogeneous compositions in their respective regions, indicating fast diffusion times of equilibration characteristic of the liquid state. In separate melting experiments on oxidized stoichiometric FeSi, we observed a similar phenomenon to the SiO₂ formation in ref. 7. A pronounced gradient of silicon moving toward the melt spot and iron moving away from the hotspot suggests this may be an artifact caused by Soret diffusion (*SI Appendix*, Fig. S3).

Our observations are consistent with multianvil experiments on ternary iron-light element systems wherein quenching from miscible conditions results in micrometer-level chemical heterogeneity, whereas quenching from immiscible conditions results in chemical heterogeneity on the 10- to 100-µm level and egg-type core structures (13). Compositional differences between two liquids cause an interfacial tension gradient so that the droplets move toward an area with lower interfacial energy under Marangoni motion (14). The driving force for separation in the LHDAC is a temperature gradient, which is typical of LHDAC experiments (i.e., ref. 15) (Fig. 1 *E* and *F*). Liquid phase separation is common in complex metal alloy sys-

tems at room pressure (16, 17) but is less well documented at high pressures. High-pressure immiscibility has been previously observed in the Fe-FeO (18) binary system. Adding a ternary component increases likelihood of phase separation (19), and immiscibility has been observed at room pressure in the Fe-Si-S (13, 19), Fe-O-S (18), Fe-C-S (19), and Fe-Si-O systems (20), which are all relevant mixtures when considering Earth's core.

While immiscibility in fluids, such as hydrogen and helium (21) or hydrocarbons (22), has been investigated at high pressures using a DAC, to our knowledge, immiscibility in iron alloy systems has not. High-pressure metal immiscibility studies have been limited to conditions achievable by large-volume experiments. The sulfur-containing systems Fe-O-S and Fe-S-Si have miscibility gaps that narrow significantly with pressure and close by 21 GPa and 15 GPa, respectively (18, 23). However, the miscibility gap in the Fe-FeO system remains roughly constant over the 15- to 21-GPa range explored (18). The Fe-Si-O system appears to behave similarly to that of the Fe-FeO at high pressures, with a roughly constant miscibility gap over the 13- to 78-GPa pressure range we investigate experimentally. Since there is no liquid immiscibility in the Fe-FeSi system, we infer that a small amount of O induces immiscibility in the Fe-Si-O system. The Fe-Si-O liquid ternary at room pressure exhibits four regions: (i) coexisting metallic liquid and solid SiO₂; (ii) coexisting metallic liquid, oxygen-rich liquid, and solid SiO₂; (iii) immiscible metallic liquid and oxygenrich liquid; and (iv) a single Fe-Si-O liquid composition (19). Our results suggest that the top of the outer core may lie in the region with immiscible metallic liquid and oxygen-rich liquid.

We performed FPMD simulations on the Fe-Si-O system at core conditions to test the behavior of silicon and oxygen in molten iron (*SI Appendix*, Table S1). We examined the Fe-8wt%Si-2wt%O system at a pressure condition similar to that in our experiments (52–53 GPa) at 3,000 K and 6,000 K and a pressure condition in the shallow outer core (140–144 GPa) at 4,500 K and 8,000 K and found liquid phase separation between Fe-Si and Fe-Si-O as observed in our experiments. While no absolute measure exists for defining immiscible alloys in ab initio simulations, we use three indirect, distinct metrics to infer immiscibility: atom trajectories, oxygen clustering, and the evolution of atom–atom coordination numbers. When taken together, the metrics suggest immiscibility occurs at low temperatures above melting, while the miscibility gap is overcome at high temperatures.

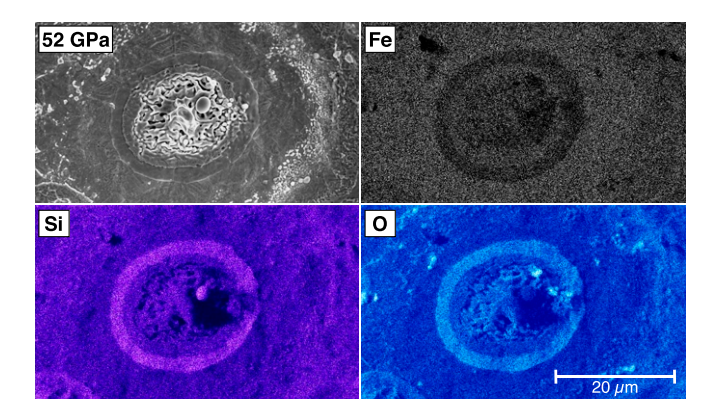


Fig. 2. SEM image using secondary electrons of hotspot FeSi918s3 for an Fe-9wt%Si-3wt%O sample heated with KBr at 52 GPa. EDS composition maps show distribution of iron, silicon, and oxygen. Quenched textures reveal separation into a liquid shell rich in silicon and oxygen and a liquid central region depleted in silicon and oxygen (*SI Appendix*, Table S3).

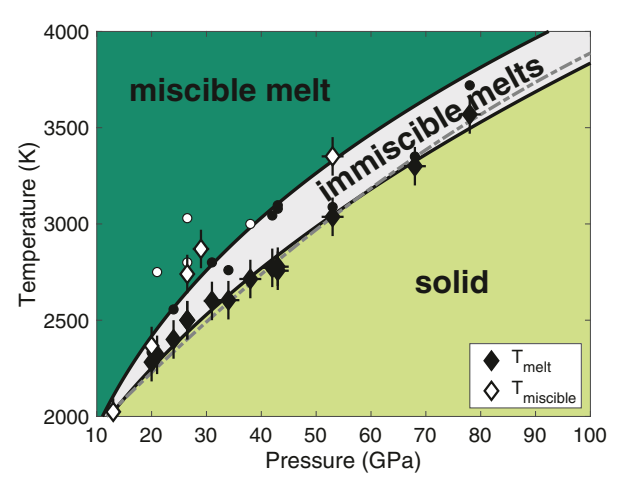


Fig. 3. Experimental results for observed miscibility regions in an Fe-9wt%Si-3wt%O alloy based on textural evolution of the melt spot. Diamonds represent the perimeter temperatures which enclose the dispersed microstructure texture indicating miscibility (white) and egg-type core microstructure texture indicating immiscibility (black), respectively. White circles (dispersed microstructure) and black circles (egg-type core microstructure) represent maximum temperatures recorded in the melt regimes and allow for tighter bounds on the miscibility closure curve. The gray dasheddotted line is the melting curve of Fe-9wt%Si from an independent study (12). Sample details can be found in SI Appendix, Table S2.

One gauge of the relative miscibility with temperature is the tendency for oxygen atoms to cluster with each other, forming distinct Fe-Si-O domains and leaving regions with only Fe-Si (Fig. 4). At 53 GPa and 3,000 K, oxygen trajectories leave significant void spaces in the simulation cell, but at 6,000 K, the oxygen fills the simulation cell (SI Appendix, Fig. S4). The clustering activity can be also understood in terms of the oxygen-oxygen coordination. At 3,000 K, about 80% of the oxygen atoms (that is, 11 of a total of 14 oxygen atoms in this simulated system) are coordinated with each other via O-Fe/Si bonding, with the majority being in two-, three-, and fourfold states (SI Appendix, Fig. S5). These coordinated oxygen atoms together can represent one or more clusters, which can be identified and counted over the entire simulation duration. Our cluster analysis shows that six or more oxygen atoms cluster over 50% of the time in the melt. However, such recognizable clusters are almost absent at 6,000 K, consistent with low abundances of two- and threefold coordination species. A similar phenomenon is seen at 144 GPa at 4,500 K when oxygen tends to cluster, but at 8,000 K, oxygen explores the simulation cell more evenly and forms no clusters of six or more atoms. As temperature increases, the Fe-Si-O composition thus becomes more dilute in O as the compositions of the Fe-Si and Fe-Si-O liquids evolve toward a single liquid such that the amount of oxygen atoms coordinated with two or more oxygen atoms decreases (Fig. 4 and SI Appendix, Fig. S5).

It is relevant to note that both Fe-Si-O and Fe-Si domains are prevalent in the melt at all conditions. Our structural analysis shows that an oxygen atom which is bonded with a silicon atom is always bonded with one or more iron atoms. All silicon atoms are highly coordinated with iron atoms, but only about one-fourth of them are also bonded with oxygen (SI Appendix, Figs. S6 and S7). The remaining area includes only Fe-Si bonding, indicating oxygen-free Fe-Si domains. As discussed in the previous paragraph, these Fe-Si-O and Fe-Si domains tend to cover extended distinct volumes, thereby implying liquid phase separation at modest temperatures above melting (Fig. 4). Notably, none of the silicon atoms are more than threefold coordinated with oxygen and hence not characteristic of solid SiO₂ or liquid SiO₂ at core conditions (24, 25) (SI Appendix, Figs. S6 and S7), consistent with the inability to crystallize SiO2 out of metallic melt in our experiments.

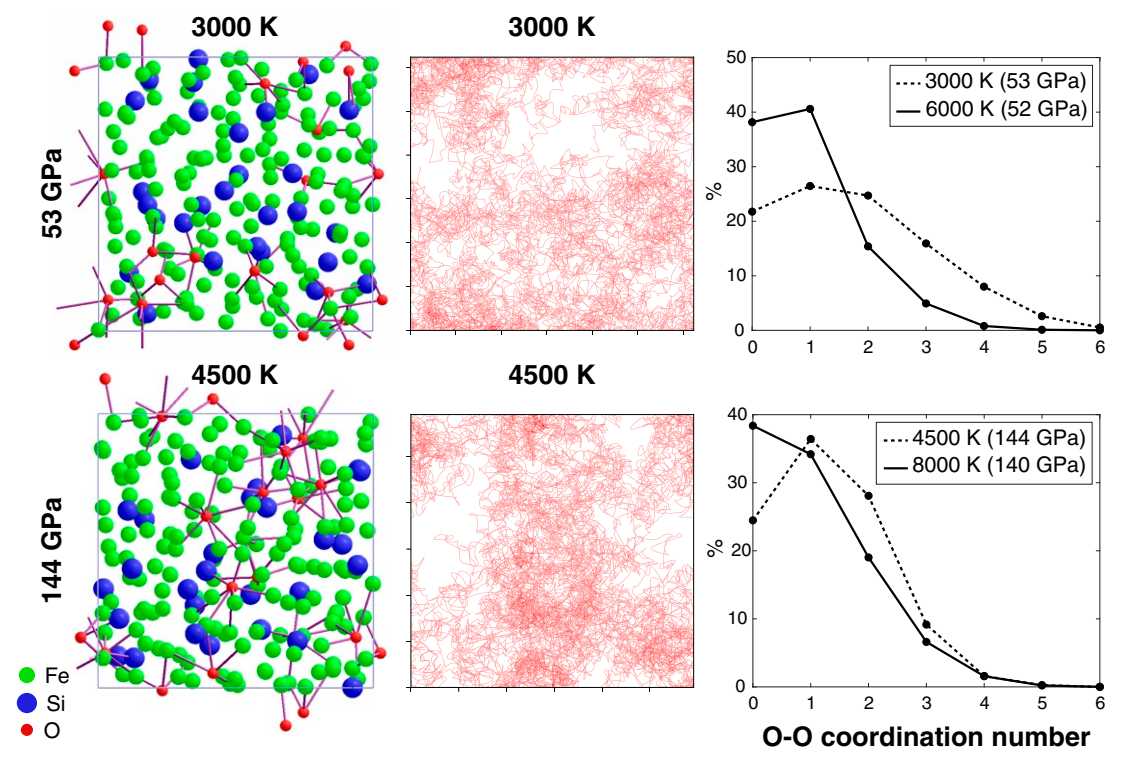


Fig. 4. Visualization snapshots (Left) and oxygen trajectories (Center) of the simulated Fe₁₅₈Si₂₈O₁₄ system (8 wt% Si, 2 wt% O) at two conditions. (Right) Plots compare the O-O coordination distributions between low and high temperatures at two pressures.

We also performed simulations in a near-equal molar ratio Fe-Si-O system (Fe-27wt%Si-16wt%O) to demonstrate that the phenomenon of liquid phase separation holds for other Fe-Si-O compositions, and the phase separation is more pronounced with increasing concentrations of Si and O (SI Appendix, Figs. S8-\$10). The overall coordination numbers are larger than that of the Fe-8wt%Si-2wt%O system for all atom pairs due to the increased abundance of Si and O relative to Fe. Even so, the average O-O coordination number also decreases with increasing temperature for the near-equal ratio of the Fe-Si-O system, indicative of miscibility gap closure. Additionally, the Si-O coordination for the near-equal ratio of the Fe-Si-O system exhibits \sim 8% sixfold coordination at 4,000 K and 125 GPa, but less than 1% at 6,000 K at 146 GPa, indicating that silicon and oxygen are not saturated in the melt and therefore solid SiO₂ will not precipitate. Rather than observing domains of Fe-Si-O and Fe-Si, the Fe-27wt%Si-16wt%O system exhibits liquid domains of Fe-Si, Fe-Si-O, and Si-O at modest temperatures above melting, reminiscent of the complex ambient-pressure Fe-Si-O

A stratified layer at the top of Earth's outer core, dubbed the E' layer, has been predicted for several decades based on robust seismic observations of low compressional wave velocities compared with the bulk of the outer core (26). Speculations about the thickness of the layer vary widely, ranging from 2 km to 800 km thick (27-29) due to strong tradeoffs with density contrasts. Stability of the layer implies that it is less dense than the bulk of the outer core. The means of formation of a stably stratified layer are widely debated and range from barodiffusion of light elements from inner core solidification (30), to a layer enriched in mantle material through chemical reactions at the core-mantle boundary (31), to an impactor core that did not fully mix with Earth's protocore and became stratified (32). Thermodynamic modeling of the liquid Fe-O-S system suggested immiscibility persists at core pressures, but was discounted as a mechanism for generating the E' layer due to a nonobservation of internal reflections below the CMB (27). Since then, there have been more robust measurements from body wave seismology of E' as an anomalously slow region (26, 29, 33-35). It should be noted that a recent seismological normal mode analysis, by allowing deviations from existing global seismic models, suggested that an anomalously slow region is not needed to explain the seismic profile through the outer core (36), but the study also does not preclude the existence of a layered

Minor density contrasts between the E' layer and the bulk outer core are enough to stably stratify the layer (30, 37), but simply enriching the amount of light elements in the E' layer cannot explain its anomalously low velocity. Simultaneously satisfying low density and low seismic velocities requires invoking other mechanisms, such as having different light elements present in the E' layer compared with the bulk outer core (38). Immiscibility in Fe-Si-O may provide separation into a bulk outer core and a buoyant, slow stratified layer. However, we see that silicon partitions evenly or slightly more into the oxygen-rich liquid (SI Appendix, Table S3), which would lead to a stratified layer that is enriched overall in light elements and hence with velocities higher than the bulk outer core. Thus, another light element species which partitions favorably into the oxygendepleted liquid phase is required to satisfy a slow layer atop the core.

If immiscibility persists to core pressures as suggested by experimental evidence and extrapolated by first-principles calculations, the miscibility gap dictates the evolution of layers in the core as it cools (Figs. 3 and 5). Three different scenarios are possible as the system moves to high pressures >136 GPa deep in the core and are illustrated in Fig. 5. (i) The geotherm lies entirely in the miscible regime, and the core liquid is a homogeneous

mixture of Fe-Si-O (Fig. 5A). This example uses a representative endmember hot core geotherm (39) before nucleation of the inner core. (ii) The geotherm intersects the miscibility closure curve within the core (Fig. 5B). In this case, the Fe-Si and Fe-Si-O will demix first from the bottom of the core. The Fe-Si-O from deep within the core will buoyantly rise and remix with Fe-Si-O as it crosses back into the stability region at the top of the core, enriching the uppermost layer of Fe-Si-O. This process of demixing and remixing continues until all of the oxygen is concentrated in the stratified layer or until the geotherm stabilizes in the immiscible regime. In this regime, the thickness of the stratified layer is subject to growth and reduction during dynamic demixing and remixing which is represented by a flexible layer boundary in Fig. 5B. (iii) The geotherm lies entirely in the immiscible regime, and the core remains as two separate layers of Fe-Si and Fe-Si-O (Fig. 5C). This example uses a "cold" core geotherm in which our melting curve is extrapolated using the melting temperature of pure iron to pin the inner-core boundary (ICB) temperature [note the extrapolated melting curves of pure iron and Fe-Si9wt% are indistinguishable at these pressures (12, 40)]. This cold core geotherm is not the lower bound for a core geotherm in general, but it is the cold endmember for our case of an of Fe-Si-O outer core which has a high melting temperature.

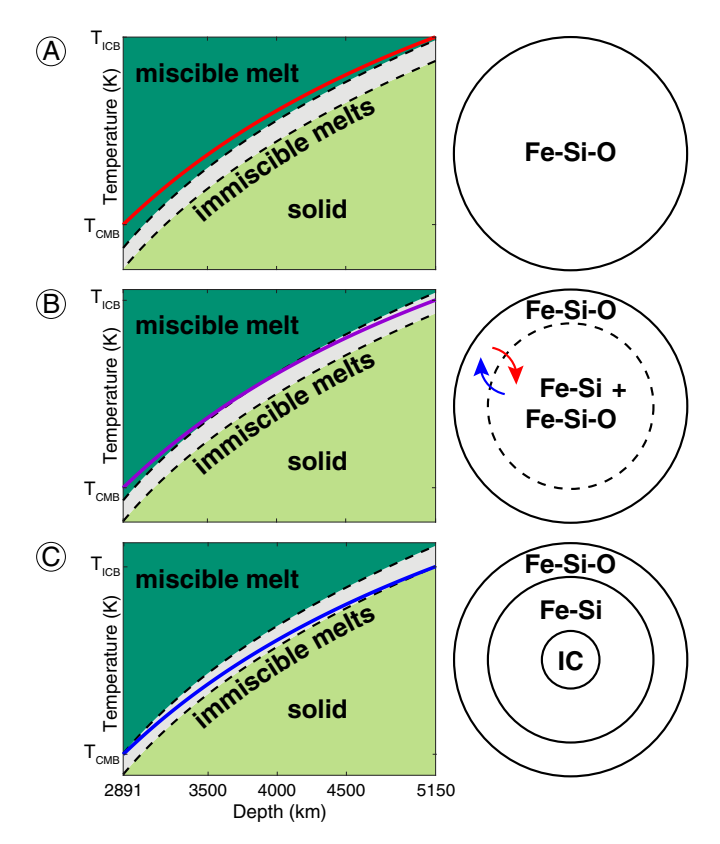


Fig. 5. Curves extrapolated to the present-day liquid core region from the core–mantle boundary (2,891 km) to the inner-core boundary (5,150 km) and corresponding schematic core structure. (A) A hot geotherm which falls entirely in the range of Fe-Si-O miscibility would suggest a homogeneous molten core. (B) An intermediate geotherm that intersects the miscibility closure curve would suggest a fully molten core with the interior portion composed of immiscible Fe-Si-O and an outer portion of miscible Fe-Si-O. The dashed circle represents a temporally changing depth that corresponds to the intersection of the geotherm with the miscibility closure where there will be demixing and remixing (represented by blue and red arrows, respectively) between the layers. (C) A cold geotherm which falls entirely in the range of Fe-Si/Fe-Si-O immiscibility and intersects the melting curve at the ICB such that the inner core exists at its present size.

Because the core geotherm cooled over time, thermal evolution of the core may also cause the geotherm to traverse back and forth through the different regimes temporally. When inner-core crystallization initiates and begins to preferentially incorporate some light elements in the solid, the process of demixing may be further complicated.

The thickness of the resulting stratified layer depends on the initial silicon and oxygen content of the core and on which of the three scenarios is realized. For instance, for an initial composition with 6 wt% silicon and 1 wt% oxygen that matches the density from Preliminary Reference Earth Model (PREM) at the core–mantle boundary (38, 41), a core like in scenario 3

at the core–mantle boundary (38, 41), a core like in scenario 3 (Fig. 5C) wherein $K_{Si}^{liq} = \frac{x_{Si}^{layer}}{x_{Si}^{bulk}} = 1$ and $K_{O}^{liq} = \frac{x_{O}^{layer}}{x_{O}^{bulk}} = 10$ results in a 700-km-thick stratified layer that has an $\sim 1.7\%$ density contrast compared with the bulk outer core (*SI Appendix*). The strong partitioning of oxygen into the buoyant layer results in large density contrasts > 3% for core oxygen budgets of > 2%. Such strong density contrasts would lead to strong reflections off the bottom layer boundary which are not observed seismically.

Immiscibility in the Fe-Si-O system simultaneously provides new constraints on outer core composition and may explain a stratified layer atop the outer core. Earth's magnetic field is generated in the liquid outer core and is sensitive to compositional differences (42), so time-dependent demixing and remixing caused by immiscibility present in iron alloy liquids may explain variations in paleomagnetic field intensities. Further studies of immiscibility in molten alloys at high pressures will shine light upon the composition and structure of Earth's core and planetary cores more generally.

Materials and Methods

Samples. Fe-Si9wt% powder (Goodfellow; FE166012, 99.9% purity) or stoichiometric FeSi powder (Alfa Aesar; 14019, 99.9% purity) was pressed into a thin foil 5–10 μm thick. The foil represents a single grain $\sim\!\!15~\mu m$ in diameter.

High-Pressure and High-Temperature Experiments. We used LHDACs equipped with 300-μm or 200-μm culets for experiments performed between 13-50 GPa and 50-78 GPa, respectively (SI Appendix, Fig. S1). The sample foils were loaded into preindented rhenium gaskets 15–30 $\,\mu m$ thick using double-sided stepped anvils (43). Either KBr or Ar was used as a pressure-transmitting medium and as an insulation medium. In the salt-insulated experiments, 5- to 10- μm discs of KBr (Intl. Crystal Laboratories; 99.95% purity) were loaded above and below the metal foil, and the assembly was dried in an oven at 400 K for at least 1 h before compression. In the noble gas-insulated experiments, 5–10 μm of liquid Ar was loaded cryogenically above and below the metal foil. Pressure was measured before and after heating using the Raman edge shift of diamond (44). Pressures reported in Fig. 3 represent pressure after quenching from high temperature, and error bars represent a combination of change in pressure from before heating and pressure gradients in the DAC. We did not account for thermal pressure.

Samples were subjected to single-sided ramp heating (45) with a 1,070-nm fiber continuous wave laser (SPI 100 W CWM). Each sample was annealed at a low laser power for 2 s, ramped to a peak power in 1 s, and held at the peak power for 1 s before the laser was shut off. A 2D temperature map was measured at the peak temperature using the four-color method (46). We ascribed a temperature error of 100 K to our reported peak temperatures (SI Appendix, Table S2) which includes measurement error stemming from calibrations and corrections, spatial resolution of melt bleb

texture and corresponding temperature map, differences between multiple measurements, and error due to Wien fitting. Details on temperature measurement and accuracy can be found in ref. 46. Melting-point data (Fig. 3) were confirmed by the integration of hundreds of pixels on multiple spots for a given sample, yielding standard deviations of 10–50 K which are included in the aforementioned error analysis. Care was taken to include only data that did not experience runaway heating that can occur at temperatures near the melting point of KBr (SI Appendix, Fig. S11) (47. 48).

Chemical Analyses. Recovered samples were analyzed by a scanning electron microscope (SEM) (Phillips XL-30 ESEM) and an electron probe microanalyzer (EPMA) (JEOL JXA-8530F) in the Yale University Department of Geology & Geophysics. To investigate the compositions of the quenched melts and unheated starting alloys, samples were interrogated both in map view and in cross-section. We used the focused ion beam (FIB) to cut the samples in cross-section (45) and samples were coated with carbon and analyzed by energy- or wavelength-dispersive spectroscopy (EDS or WDS) to determine chemical composition. The EPMA is equipped with five wavelength-dispersive spectrometers using layered diffracting elements (LDE1), thallium acid pthalate (TAP), pentaerythritol (PET), and lithium fluoride (LIF) diffracting crystals. Fe and Re were referenced to metal standards and Si and O to oxides. Analytical conditions were 10 kV, giving an approximate analytical volume of 1 μ m³, a 15-nA beam current, and a beam spot size of 1 μm . X-ray counts were acquired on peak for 20 s or 22 s and off peak for the same total times. Small melt volumes prevented acquisition of robust quantitative WDS measurements within different melt regions for most samples. Attempts to do so are shown in SI Appendix, Table S3.

The unheated starting material in quenched samples using KBr as insulation has an oxygen content of $\sim \! 3$ wt% as measured by WDS (SI Appendix, Tables S1–S3). The Ar provides a more oxygen-poor environment than KBr does, and quenched samples have an oxygen content of $< \! 1$ wt% as measured by WDS (SI Appendix, Tables S1 and S3). The source of oxygen is likely from air contamination. While oxidation initially affects the surface of the metal foil, annealing the sample at a low laser power for $\sim \! 10$ s overcomes diffusion timescales and allows for homogenization of the starting material. Recovered samples showed no reaction with the insulation media or the Re qasket.

First-Principles Molecular Dynamics Simulations. FPMD simulations were carried out using the VASP software (49) in the NVT-canonical ensemble (with temperature controlled with a Nosé thermostat) with periodic boundary conditions. The projector augmented wave potentials (50, 51) were used together with the generalized gradient approximation (GGA) of the exchange-correlation potential (52). The plane-wave basis set cutoff used was 400 eV, which resulted in Pulay stress of \sim 1-4 GPa. Brillouin zone sampling was performed only at the Gamma point. We ran simulations for 6.6-20 ps with a time step of 1 fs. We simulated the Fe-Si-O system for two compositions: Fe₁₅₈Si₂₈O₁₄ and Fe₈₈Si₈₄O₈₄ (SI Appendix). In each case, the system was initially melted and thermalized at 8,000 K or 6,000 K and then subsequently guenched down to desired lower temperatures. The calculated radial distribution functions (RDFs) show the presence of short-range order but no long-range disorder as expected for a liquid state (SI Appendix, Fig. \$12). The detailed structural analysis was performed using the visualization system of ref. 53.

ACKNOWLEDGMENTS. We thank Jim Eckert, Fernando Camino, and Jennifer Girard for experimental assistance. We thank Louisiana State High-Performance Computing and the Yale Center for Research Computing for guidance and use of the research computing infrastructure, specifically Kaylea Nelson. This work was funded by the NSF Grant (EAR-1551348 and EAR-1764140) and a NASA Connecticut Space Grant (to S.M.A.) (Federal Award NNX15AI12H). This research used resources of the Center for Functional Nanomaterials, which is a US Department of Energy Office of Science Facility, at Brookhaven National Laboratory under Contract DE-SC0012704. Electron microscopy with EDS/WDS was funded by the NSF Grant (EAR-0744154) and Yale University.

^{1.} Hirose K, Labrosse S, Hernlund J (2013) Composition and state of the core. *Annu Rev Earth Planet Sci* 41:657–691.

^{2.} Birch F (1952) Elasticity and constitution of the Earth interior. J Geophys Res 57:

Hirose K, Labrosse S, Hernlund J (2001) Solubility of silicon in liquid metal at high pressure: Implications for the composition of the Earth's core. Earth Planet Sci Lett 184:367–376

MacDonald GJF, Knopoff L (1958) On the chemical composition of the outer core. Geophys J R Astron Soc 1:284–297.

Alfe D, Gillian MJ, David Price G (2002) Composition and temperature of the Earth's core constrained by combining ab initio calculations and seismic data. Earth Planet Sci Lett 195:91–98.

Badro J, Cóté AS, Brodholt JP (2014) A seismologically consistent compositional model of Earth's core. Proc Natl Acad Sci USA 111:7542–7545.

Hirose K, et al. (2017) Crystallization of silicon dioxide and compositional evolution of the Earth's core. Nature 543:99–102.

^{8.} Fischer RA, et al. (2015) High pressure metal-silicate partitioning of Ni, Co, V, Cr, Si, and O. *Geochimica et Cosmochimica Acta* 167:177–194.

- Rubie DC, et al. (2015) Accretion and differentiation of the terrestrial planets with implications for the compositions of early-formed solar system bodies and accretion of water. *Icarus* 248:89–108.
- Wang CP, Liu XJ, Ohnuma I, Kainuma R, Ishida K (2002) Formation of immiscible alloy powders with egg-type microstructure. Science 297:990–993.
- Porter DA, Eastering KE, Sherif MY (2009) Phase Transformations in Metals and Alloys (CRC Press LLC, Boca Raton, FL), pp 300–308.
- Fischer RA, et al. (2013) Phase relations in the Fe-FeSi system at high pressures and temperatures. Earth Planet Sci Lett 373:54–64.
- Morard G, Katsura T (2010) Pressure-temperature cartography of Fe-S-Si immiscible system. Geochim Cosmochim Acta 74:3659–3667.
- Marangoni C (1871) Über die ausbreitung der tropfen einer flussigkeit auf der oberfläche einer anderen [Spreading of droplets of a liquid on the surface of another]. Annalen der Physik [Ann Phys Chem] 219:337–354.
- Kavner A, Panero WR (2004) Temperature gradients and evaluation of thermoelastic properties in the synchrotron-based laser-heated diamond cell. *Phys Earth Planet Interiors* 143:527–539.
- Tersoff J (1995) Surface-confined alloy formation in miscible systems. Phys Rev Lett 74:434–437.
- Butt M, Bodsworth C (1991) Liquid immiscibility in ternary metallic alloys. Mater Sci Technol 7:795–802.
- Tsuno K, Ohtani E, Terasaki H (2007) Immiscible two-liquid regions in the Fe-O-S system at high pressure: Implications for planetary cores. Phys Earth Planet Interiors 160:75–85.
- 19. Raghavan V, Raynor GV, Rivlin VG (1987) Phase Diagrams of Ternary Iron Alloys (Indian Institute of Metals, Calcutta, India).
- Fabrichnaya OB, Sundman B (1997) The assessment of thermodynamic parameters in the Fe-O and Fe-Si-O systems. Geochim Cosmochim Acta 61:4539–4555.
- Loubeyre P, Letoullec R, Pinceaux JP (1987) Binary phase diagrams of H-2-He mixtures at high-temperature and high-pressure. Phys Rev B 36:3723–3730.
- Huang F, Daniel I, Cardon H, Montagnac G, Sverjensky DA (2017) Immiscible hydrocarbon fluids in the deep carbon cycle. Nat Commun 8:15798.
- Sanloup C, Fei Y (2004) Closure of the Fe-S-Si liquid miscibility gap at high pressure. Phys Earth Planet Interiors 147:57–65.
- 24. Millot M, et al. (2015) Shock compression of stishovite and melting of silica at planetary interior conditions. *Science* 347:418–420.
- Karki BB, Bhattarai D, Stixrude L (2007) First-principles simulations of liquid silica: Structural and dynamical behavior at high pressure. Phys Rev B 76:104205.
- 26. Garnero EJ, Helmberger DV, Grand SP (1993) Constraining outermost core velocity
- with SmKS waves. *Geophys Res Lett* 20:2463–2466.

 27. Helffrich G, Kaneshima S (2004) Seismological constraints on core composition from
- Fe-O-S liquid immiscibility. *Science* 306:2239–2242.

 28. Helffrich G (2014) Outer core compositional layering and constraints on core liquid
- transport properties. *Earth Planet Sci Lett* 391:256–262.

 29. Tang V, Zhao L, Hung SH (2015) Seismological evidence for a non-monotonic velocity
- gradient in the topmost outer core. Sci Rep 5:8613.
 30. Gubbins D, Davies CJ (2013) The stratified layer at the core-mantle boundary caused by barodiffusion of oxygen, sulphur and silicon. Phys Earth Planet Interiors 215:21–28.
- Buffett BA, Seagle CT (2010) Stratification of the top of the core due to chemical interactions with the mantle. J Geophys Res 115:B04407.

- 32. Landeau M, Olson P, Deguen R, Hirsh BH (2016) Core merging and stratification following giant impact. *Nat Geosci* 9:786–790.
- Tanaka S (2007) Possibility of a low P-wave velocity layer in the outermost core from global SmKS waveforms. Earth Planet Sci Lett 259:486–499.
- Helffrich G, Kaneshima S (2010) Outer-core compositional stratification from observed core wave speed profiles. Nature 468:807–812.
- 35. Kaneshima S, Matsuzawa T (2015) Stratification of Earth's outermost core inferred from SmKS array data. *Prog Earth Planet Sci* 2:9.
- Irving JC, Cottaar S, Lekić V (2018) Seismically determined elastic parameters for Earth's outer core. Sci Adv 4:eaar2538.
- Helffrich G, Kaneshima S (2013) Causes and consequences of outer core stratification. Phys Earth Planet Interiors 223:2–7.
- Brodholt J, Badro J (2017) Composition of the low seismic velocity E layer at the top of Earth's core. Geophys Res Lett 44:8303–8310.
- 39. Williams Q, Gurnis M, Wysession ME, Knittle E, Buffett BA (1998) Core-Mantle Boundary Region (American Geophysical Union, Washington, DC), pp 73–81.
- Anzellini S, Dewaele A, Mezouar M, Loubeyre P, Morard G (2013) Melting of iron at Earth's inner core boundary based on fast x-ray diffraction. Science 340:464.
- 41. Dziewonski AM, Anderson DL (1981) Preliminary reference Earth model. *Phys Earth Planet Interiors* 25:297–356.
- 42. Jacobson SA, Rubie DC, Hernlund J, Morbidelli A, Nakajima M (2017) Formation stratification, and mixing of the cores of Earth and Venus. *Earth Planet Sci Lett* 474:375–386.
- 43. Du Z, et al. (2015) Using stepped anvils to make even insulation layers in laser-heated diamond-anvil cell samples. *Rev Sci Instrum* 86:095103.
- Akahama Y, Kawamura H (2004) High-pressure Raman spectroscopy of diamond anvils to 250 GPa: Method for pressure determination in the multimegabar pressure range. J Appl Phys 96:3748–3751.
- 45. Du Z, Lee KKM (2014) High-pressure melting of MgO from (Mg, Fe)O solid solutions. Geophys Res Lett 41:8061–8066.
- Du Z, Amulele G, Benedetti LR, Lee KKM (2013) Mapping temperatures and temperature gradients during flash heating in a diamond-anvil cell. Rev Sci Instrum 84:075111.
- Arveson SM, Kiefer B, Deng J, Lee KKM (2018) Thermally induced coloration of KBr at high pressures. Phys Rev B 97:094103.
- Boehler R, Ross M, Boercker DB (1996) High-pressure melting curves of alkali halides. *Phys Rev B* 53:556–563.
- Kresse G, Furthmuller J (1996) Efficiency of ab-initio total energy calculations for metals and semiconductors using a plane-wave basis set. Comput Mater Sci 6:15–50.
- Kresse G, Joubert D (1999) From ultrasoft pseudopotentials to the projector augmented wave method. Phys Rev B 59:1758–1775.
- Blöchl PE, Jepsen O, Andersen OK (1999) Improved tetrahedron method for brillouin zone integrations. Phys Rev B 49:16223–16233.
- Perdew JP, Burke K, Ernzerhof M (1996) Generalized gradient approximation made simple. Phys Rev Lett 77:3865–3868.
- Bhattarai D, Karki BB (2009) Atomistic visualization: Space-time multiresolution integration of data analysis and rendering. J Mol Graphics Model 27: 951–968